

Generalized Terrain Topography in Radar Scattering Models

Mariko S. Burgin, *Member, IEEE*, Uday K. Khankhoje, *Member, IEEE*, Xueyang Duan, *Member, IEEE*, and Mahta Moghaddam, *Fellow, IEEE*

Abstract—Modeling of terrain topography is crucial for vegetated areas given that even small slopes impact and alter the radar wave interactions between the ground and the overlying vegetation. Current missions either exclude pixels with large topographic slopes or disregard the terrain topography entirely, potentially accumulating substantial modeling errors and therefore impacting the retrieval performance over such sloped pixels. The underlying terrain topography needs to be considered and modeled to obtain a truly general and accurate radar scattering model. In this paper, a flexible and modular model is developed: the vegetation is considered by a multilayered multispecies vegetation model capable of representing a wide range of vegetation cover types ranging from bare soil to dense forests. The ground is incorporated with the stabilized extended boundary condition method, allowing the representation of an N -layered soil structure with rough interfaces. Terrain topography is characterized by a 2-D slope with two tilt angles (α, β). Simulation results for an evergreen forest show the impact of a 2-D slope for a range of tilt angles: a 10° tilt in the plane of incidence translates to a change of up to 15 dB in HH, 10 dB in VV, and 1.5 dB in HV for the total radar backscatter. Terrain topography is shown to be crucial for accurate forward modeling, especially over forested areas.

Index Terms—Electromagnetic scattering, modeling, radar terrain factors, remote sensing, vegetation.

I. INTRODUCTION

TERRAIN topography is a first-order determinant of how water flows through hill slopes. Consequently, it impacts the spatial distribution of geophysical parameters such as soil moisture and, more indirectly, vegetation and surface/canopy temperature. However, topography also directly alters the local incidence angle and, therefore, the radar wave interactions between the ground and overlying vegetation. It is well known that a sloped terrain greatly impacts both active [1] and passive [2] microwave remote sensing measurements. Most existing radar models do not consider terrain topography, and geophysical pa-

rameters such as soil moisture are retrieved over relatively flat pixels or pixels that can be assumed flat [3], [4]. The availability of high-resolution digital elevation maps allows the calculation of 2-D slopes for each pixel and hence enables more accurate modeling of a sloped vegetated scene.

Previous work on terrain topography effects on radar scattering includes a high-frequency electromagnetic radar scattering model for a tree trunk above a tilted ground plane by Lin and Sarabandi [5]. This model treats the trunk as a finite-length stratified dielectric cylinder with a corrugated bark, while the ground is considered as a smooth homogeneous dielectric with an arbitrary slope. The effect of the ground is implemented based on the ground surface Fresnel reflection coefficients of a smooth tilted surface. The validity of the model is investigated and discussed by simulating several cases for a tilted ground plane. The model by Lopez-Sanchez *et al.* [6] extends the previous model by introducing multiple vertical dielectric cylinders representing trunks above a dielectric rough half space according to Tsang *et al.* [7]. Smith-Jonforsen *et al.* [8] introduce a model for backscattering from forests for the very high frequency range. They model the trunks as dielectric cylinders and the ground as a homogeneous smooth dielectric half-space and address the slope by calculating the reflectivity matrix based on the Fresnel reflection coefficients and the scalar products between the local and global coordinate systems. Good agreement with measurements has been reported in that work. More recent work includes Park *et al.* [9] who studied the effect of topographic slope on microwave backscattering returns using a radiative transfer approach.

Our approach is motivated by, and substantially expands on, the work of van Zyl [10]. The terrain topography characteristic is added to our existing multispecies multilayer vegetation model that has previously been published [11]. Four scattering mechanisms are considered as shown in Fig. 1: 1) direct backscattering from the branch layer volume (B); 2) direct backscattering from the ground (G); 3) branch-ground double bounce (BG) consisting of specular crown scattering followed by rough ground reflection and vice versa; and 4) trunk-ground double bounce (TG) consisting of specular trunk scattering followed by rough ground reflection and vice versa. For the double-bounce scattering terms, two-way propagation is considered by multiplying the double-bounce Stokes matrix by the transmission matrices for transmission in both directions. For vegetated flat areas and especially forested areas, trunk-ground and branch-ground double bounce can contribute significantly to the total radar backscatter and are strong functions of the underlying topography. Due to the prominent vertical orientation of the trunk with respect to the ground for flat scenes, the trunk-ground double bounce is generally the dominant of the two

Manuscript received November 7, 2015; revised January 14, 2016; accepted February 6, 2016. Date of publication March 15, 2016; date of current version May 24, 2016. This work was supported in part by the Jet Propulsion Laboratory, California Institute of Technology, Pasadena, CA, USA, under a contract with the National Aeronautics and Space Administration.

M. S. Burgin and X. Duan are with the Jet Propulsion Laboratory, California Institute of Technology, Pasadena, CA 91109 USA.

U. K. Khankhoje is with the Indian Institute of Technology Delhi, New Delhi 110016, India.

M. Moghaddam is with the University of Southern California, Los Angeles, CA 90007 USA (e-mail: mahta@usc.edu).

Color versions of one or more of the figures in this paper are available online at <http://ieeexplore.ieee.org>.

Digital Object Identifier 10.1109/TGRS.2016.2532123

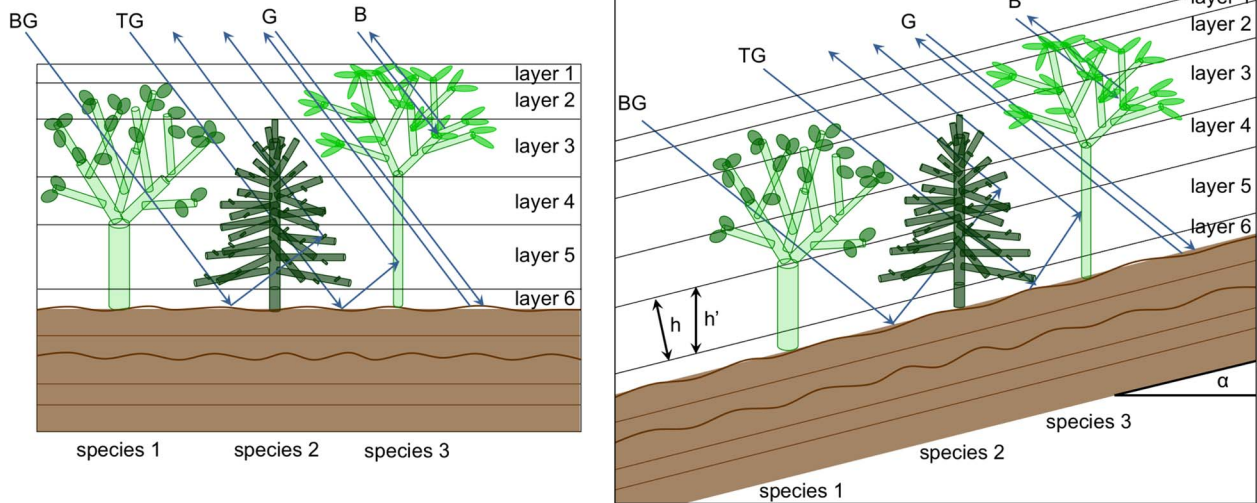


Fig. 1. Realistic forest geometry consisting of multiple species N_S and multiple layers N . Figure shown for $N_S = 3$, $N = 2 N_S$, and four scattering mechanisms for flat (left) and sloped (right) terrain. The key parameters to modify the flat to sloped terrain are the vegetation layer thickness h , the adjusted vegetation layer thickness h' , and the tilt angles ($\alpha, \beta = 0$).

scattering mechanisms since both scattering moments at the trunk and the ground are specular [12], [13].

In [10], a methodology was introduced to define topography in two dimensions by an angle α in the plane of incidence and an angle β perpendicular to the plane of incidence. This method considers the trunk to stay perpendicular to the slope, which may not be a realistic assumption. It also assumes that the trunk orientation with respect to the surface normal follows a Gaussian probability density function, and the average trunk-ground interaction is the average over this distribution; this is an arbitrary assumption and may or may not hold in general. Following the principle of geotropism, we assume the trees to grow vertically in our development. That said, the methods developed here are fully general and can be applied to any arbitrary orientation of the tree. The method can therefore handle any angle between the tree and the ground surface.

The characterization of the slope with two angles (α, β) is maintained, although with a slightly different definition. The notation used to describe the coordinate system is the forward scatter alignment (FSA) shown in Fig. 2. Introducing a topography, as an example in one dimension ($\beta = 0$), will alter the scattering moments at the trunk and the ground. There will be two major possible paths in the backscattering direction: 1) specular scattering at the trunk followed by nonspecular scattering at the ground as shown in Fig. 3(a) and (2) nonspecular scattering at the trunk followed by specular scattering at the ground as shown in Fig. 3(b). Adding another dimension of topography will render the setup more complex, but the two main scattering moments remain the same. The adjustment to take into account nonspecular scattering from the ground can be computed by using a fully coherent rough surface scattering model, in our case the Stabilized Extended Boundary Condition Method (SEBCM) [14], while the nonspecular scattering from the trunk can be computed by choosing the appropriate scattering angle of a finite dielectric cylinder representing the tree trunk. The use of the multilayer SEBCM model [14] allows the inclusion of an N -layered soil with rough interfaces. We also assume that a given pixel has homogeneous soil moisture

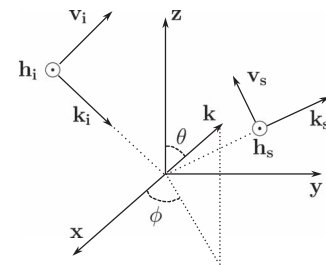


Fig. 2. Vector orientations assuming forward scattering alignment (FSA). The electric field is represented in terms of the vertical and horizontal polarization vectors, \vec{v}, \vec{h} , respectively, while the wave vector is represented by \vec{k} . The subscripts i, s represent the incident and scattered components, respectively. The angular components of any general wave vector \vec{k} are represented by polar coordinates (θ, ϕ) , as shown. The xy plane is parallel to the ground surface.

and texture composition along each slice of the profile; we note that this is not a fundamental assumption. Spatial heterogeneity in soil characterization can be implemented when computing radar backscattering as given in [15].

The novelty of this work is to construct a framework that computes the total radar backscatter coefficient given an arbitrary orientation of vegetation and terrain that might not be horizontal. When the relative angle between a tree trunk and the ground is 90° , the dominant contribution to the radar return is via a double-bounce scattering mechanism that includes a specular scattering at both the trunk and the ground. However, when the angle between tree trunk and ground changes due to topography, this specular double-bounce scattering no longer significantly contributes to the radar return. Instead, the return must be computed by considering all intermediate scattering configurations, termed the degrees of freedom of the problem, that occur between specular scattering at the trunk (but not at the ground) and specular scattering at the ground (but not at the trunk). It must be emphasized that the objective of this paper is to lay out a general methodology by which a radar forward model can be modified to incorporate the effect of terrain topography. We demonstrate the impact of terrain topography on

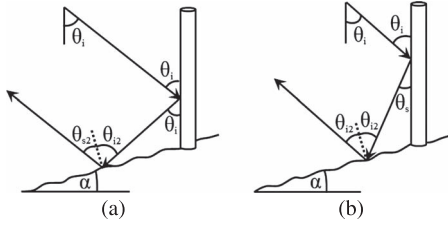


Fig. 3. Two main scattering paths for a slope described by $(\alpha, \beta = 0)$. The incidence and scattering angles are given as θ_i and θ_s . (a) Specular scattering at the trunk followed by nonspecular scattering at the ground. (b) Nonspecular scattering at the trunk followed by specular scattering at the ground.

radar backscattering by means of a set of realistic simulations within the scope of this paper.

The layout of this paper is as follows. In Section II, the impact of terrain topography on the trunk-ground double-bounce scattering mechanism is described. In Section III, the necessary model modifications are presented for each scattering mechanism, and their implementation is discussed in Section IV. In Section V, a realistic scenario inspired by the P-band Airborne Microwave Observatory of Subcanopy and Subsurface (AirMOSS) mission is set up, and simulation results are presented. This paper closes in Section VI with the conclusion.

II. IMPACT OF TERRAIN TOPOGRAPHY ON DOUBLE-BOUNCE SCATTERING MECHANISM

To better understand the impact of terrain topography, an example can be given of the trunk-ground double-bounce scattering mechanism. It can be broken down into the contributing elements, which are the respective scattering patterns of the cylinder and the ground. The scattering pattern of a (vertically oriented) finite cylinder shows a dominant return in the specular direction given by the polar angle, $\theta_s = \pi - \theta_i$, where θ_i is the radar incidence angle, while extending all around the azimuth angle ϕ . Therefore, the dominant scattering pattern of a trunk cylinder resembles a *skirt*. This is in contrast to the scattering pattern of a (horizontally oriented) rough ground, including a rough layered ground, which shows a strong specular scattering in $\theta_s = \theta_i$ and $\phi_i = \phi_s$ and resembles a *cone*. Both of these dominant scattering patterns diminish quickly if the scattering angles depart from the true specular direction. It should be noted that, although these two particular scattering paths are dominant, scattering in other directions can also occur. A visualization of the *skirt* and *cone* scattering patterns is given in Fig. 4. In the case of double-bounce scattering for a flat scene, the *skirt* and *cone* scattering patterns overlap, resulting in a strong response in the backscatter direction. Depending on the 2-D slope, the *skirt* and *cone* scattering patterns will not overlap perfectly and therefore alter—generally weaken—the overall double-bounce scattering mechanism [10].

III. FORMULATION OF SCATTERING MECHANISMS IN THE PRESENCE OF TERRAIN TOPOGRAPHY

In this section, we will formally express all scattering events, while noting that the general idea is to rotate all vectors to a “standard” frame (where the ground normal is along \hat{z}), perform the scattering events (since the scattering matrix is

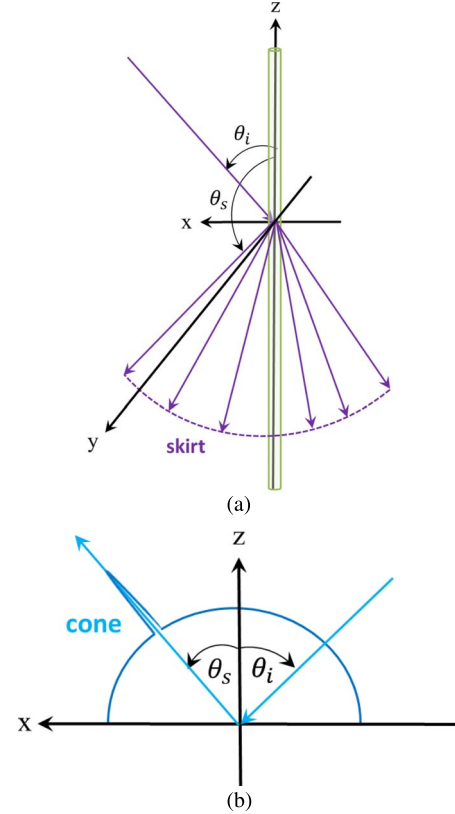


Fig. 4. Visualization of *skirt*- and *cone*-like scattering patterns. The incidence and scattering angles are given as θ_i and θ_s . (a) *Skirt*-like scattering pattern from a cylinder with $\theta_s = \pi - \theta_i$. (b) *Cone*-like scattering pattern from a rough layered ground with $\theta_s = \theta_i$.

easily expressed for the ground normal or cylinder axis being along \hat{z}), and then rotate back to the original frame.

A 2-D slope can be expressed with two parameters: angle α for a tilt in the plane of incidence (angle α in xz plane with $\alpha = 90^\circ$ rotating the x into the $-z$ -axis) and angle β for a tilt perpendicular to the plane of incidence (angle β in yz plane with $\beta = 90^\circ$ rotating the y into the z -axis) as shown in Fig. 5. We assume that the first rotation takes place within the plane of incidence (with angle α), followed by the second rotation out of the plane of incidence (with angle β). Let the unit vector \hat{g} represent the vector normal to this titled plane. Associated with these angles is a rotation matrix R , whose action is defined as follows: it rotates the normal vector to the standard z -axis, i.e., $\hat{z} = R_y(-\alpha) R_s(-\beta) = R(\alpha, \beta) \hat{g}$. The rotation matrix in (x, y, z) basis can therefore be expressed as

$$R(\alpha, \beta) = \begin{bmatrix} \cos \alpha & \sin \alpha \sin \beta & -\sin \alpha \cos \beta \\ 0 & \cos \beta & \sin \beta \\ \sin \alpha & -\cos \alpha \sin \beta & \cos \alpha \cos \beta \end{bmatrix} \quad (1)$$

where $R_s(\eta)$ and $R_y(\eta)$ are the standard rotation matrices around the x - and y -axes, respectively

$$R_x(\eta) = \begin{bmatrix} 1 & 0 & 0 \\ 0 & \cos \eta & -\sin \eta \\ 0 & \sin \eta & \cos \eta \end{bmatrix} \quad R_y(\eta) = \begin{bmatrix} \cos \eta & 0 & \sin \eta \\ 0 & 1 & 0 \\ -\sin \eta & 0 & \cos \eta \end{bmatrix} \quad (2)$$

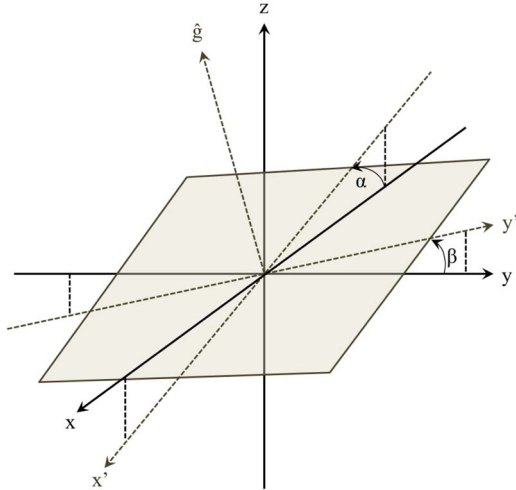


Fig. 5. Definition of slope angles (α, β) in standard coordinate system. The xy plane is parallel to the ground surface.

The inverse of this rotation matrix R^{-1} rotates the standard z -axis to the normal vector of the tilted plane, \hat{g} , i.e., $\hat{g} = R^{-1}(\alpha, \beta) \hat{z}$.

It is notable that (α, β) are the slope angles in the range (in the plane of incidence) and azimuth (out of the plane of incidence) directions, respectively, as seen from the radar. Therefore, when using radar data for validation, the regular (North, East) slope pixel definition provided with the radar data (such as, for example, for the AirMOSS P-band radar standard Level-1 processed image data, provided by the NASA Jet Propulsion Laboratory) must be converted to the (Range, Azimuth) slope definition as shown in Fig. 6.

A radar wave vector can be expressed in the spatial (x, y, z) basis or in the (right-handed, orthonormal) wave vector basis (v, h, k) . For a given orientation of a wave vector in spherical polar coordinates (θ, ϕ) , the unit vectors $(\hat{v}, \hat{h}, \hat{k})$ can be expressed in the spatial basis as

$$\begin{aligned} \hat{v} &= (-\cos\theta \cos\phi, -\cos\theta \sin\phi, \sin\theta) \\ \hat{h} &= (\sin\phi, -\cos\phi, 0) \\ \hat{k} &= (\cos\phi \sin\theta, \sin\phi \sin\theta, \cos\theta). \end{aligned} \quad (3)$$

We refer to this as the standard wave vector basis when $\hat{h} \cdot \hat{z} = 0$. If an incident wave vector has polar coordinates (θ, ϕ) , the backscattered wave vector has polar coordinates $(\pi - \theta, \phi + \pi)$. We define a matrix $P(\theta, \phi)$ that expresses a vector from the (v, h, k) basis as a vector in the (x, y, z) basis

$$P(\theta, \phi) = \begin{bmatrix} -\cos\theta \cos\phi & \sin\phi & \sin\theta \cos\phi \\ -\cos\theta \sin\phi & -\cos\phi & \sin\theta \sin\phi \\ \sin\theta & 0 & \cos\theta \end{bmatrix}. \quad (4)$$

The columns of $P(\theta, \phi)$ are the spatial components of $(\hat{v}, \hat{h}, \hat{k})$, respectively. Similarly, the $P^{-1}(\theta, \phi)$ matrix performs the reverse operation going from the (x, y, z) basis to the (v, h, k) basis. It is easy to verify that $P^{-1} = P^T$.

The four aforementioned scattering mechanisms have to be

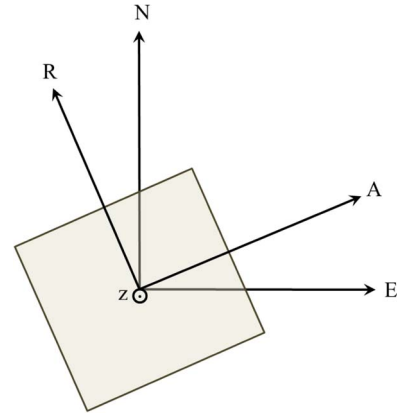


Fig. 6. Visualization of (Range, Azimuth) slope definition with respect to (North, East) slope definition as provided by standard AirMOSS Level-1 imagery.

modified for the presence of terrain topography. In the following, each of them is discussed separately:

- 1) backscatter from the branch layer structure adjusted for sloped terrain (B);
- 2) backscatter from a rough surface underlying vegetation (G);
- 3) double-bounce scattering interactions between trunks and ground (TG);
- 4) double-bounce scattering interactions between canopy (large/small branches and leaves/needles) and ground (BG).

A. Backscatter From Branch Layer Structure Adjusted for Sloped Terrain (B)

The branches in the crown layer maintain their orientation distribution regardless of the ground tilt. Therefore, the change for the backscatter from the branch canopy structure in the presence of topography is mainly an adjustment of all layer thicknesses to reflect the altered path length through each layer. This can be expressed by the new layer thickness h' as shown in Fig. 1.

$$h' = h \cdot \frac{\cos\theta_i}{\cos\beta \cos(\theta_i - \alpha)} \quad (5)$$

The adjustment of the vegetation layer thicknesses also adjusts the attenuation and transmission accordingly.

B. Backscatter From a Rough Surface Underneath Vegetation Layers (G)

In the case of the direct ground scattering, there are no degrees of freedom to be chosen. All angles are defined by the respective slope given through (α, β) . The incident wave vector is $\hat{k}_i(\theta_i, \phi_i)$, and the electric field in the (v, h, k) basis is $\vec{e}_i = (e_v^i, e_h^i, 0)$. Explicitly, the transformations that we apply to the incident electric field are as follows.

- 1) Bring \vec{e}_i into the (x, y, z) basis, i.e., apply $P(\theta_i, \phi_i)$.
- 2) Rotate the coordinate axis such that the ground is horizontal, i.e., apply $R(\alpha, \beta)$ so that the ground normal now points along \hat{z} . Also, apply the rotation to \hat{k}_i , which gives

$\hat{k}_i^g(\theta_i^g, \phi_i^g) = R(\alpha, \beta) \hat{k}_i(\theta_i, \phi_i)$, and thus the new wave vector direction (θ_i^g, ϕ_i^g) .

- 3) Bring the electric field back into the (v, h, k) basis, i.e., apply $P^{-1}(\theta_i^g, \phi_i^g)$.
- 4) Scatter the wave in the direction (θ_s^g, ϕ_s^g) , i.e., apply $S_g(\theta_s^g, \phi_s^g; \theta_i^g, \phi_i^g)$, which is the scattering matrix for a horizontal ground. The angles (θ_s^g, ϕ_s^g) must be such that, when we undo the rotation of step 2, the resulting wave vector is in the (known) backscatter direction (θ_s, ϕ_s) , i.e., $\hat{k}_s^g(\theta_s^g, \phi_s^g) = R(\alpha, \beta) \hat{k}_s(\theta_s, \phi_s)$.
- 5) Bring the electric field to the (x, y, z) basis, i.e., apply $P(\theta_s^g, \phi_s^g)$.
- 6) Undo the rotation of step 2, i.e., apply $R^{-1}(\alpha, \beta)$. This implies that the wave vector has been brought back to the backscattered direction with $\hat{k}_s(\theta_s, \phi_s) = R^{-1}(\alpha, \beta) \hat{k}_s^g(\theta_s^g, \phi_s^g)$.
- 7) Finally, bring the electric field back to the (v, h, k) basis, i.e., apply $P^{-1}(\theta_s, \phi_s)$.

Thus, the scattered electric field $\vec{e}_s = (e_v^s, e_h^s, 0)$ is given by the following sequence of matrix multiplications:

$$\vec{e}_s = \{P^{-1}(\theta_s, \phi_s) R^{-1}(\alpha, \beta) P(\theta_s^g, \phi_s^g) S_g(\theta_s^g, \phi_s^g; \theta_i^g, \phi_i^g) \cdot P^{-1}(\theta_i^g, \phi_i^g) R(\alpha, \beta) P(\theta_i, \phi_i)\} \vec{e}_i. \quad (6)$$

Generally, the angular components of a rotated wave vector can be found by the following technique. Consider a wave vector $\hat{k}(\theta, \phi)$, which has been rotated by $R(\alpha, \beta)$ to a new wave vector $\hat{k}'(\theta', \phi')$

$$\hat{k}'(\theta', \phi') = R(\alpha, \beta) \hat{k}(\theta, \phi). \quad (7)$$

By using (3), the new rotated angles can be found by the following equations:

$$\tan \phi' = \frac{k'_y}{k'_x} \quad \cos \theta' = k'_z. \quad (8)$$

The effect of these modifications is essentially the same as adjusting the incidence angle, but this treatment is more systematic and consistent with the modifications to the other scattering mechanisms.

C. Double-Bounce Scattering Interactions Between the Cylinder and the Ground (TG and BG)

The same technique is applicable to the trunk-ground (TG) and branch-ground (BG) double-bounce scattering contributions. In the case of the double bounce, there are two degrees of freedom: the polar angles (μ, τ) determine the scattering angles from the cylinder and specify an intermediate wave vector $\hat{k}(\mu, \tau)$ between the cylinder and the ground. A visualization of the scattering angles (μ, τ) from the cylinder is shown in Fig. 7(a).

The following procedure describes the double-bounce interaction in the general case of an arbitrarily oriented cylinder. Assume that the axis of the cylinder points in the angular direction given by $\hat{c} = (\gamma, \delta)$ as shown in Fig. 7(b), associated with which is a rotation matrix $R(\gamma, \delta)$ similar to (1), which rotates the cylinder axis to the standard z -axis, i.e., $\hat{z} =$

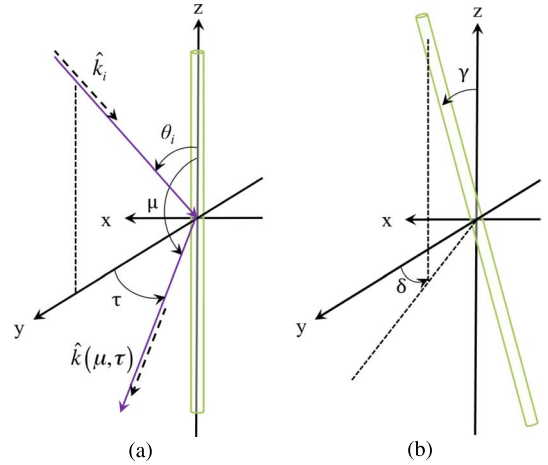


Fig. 7. Visualization of angles (μ, τ) and (γ, δ) . (a) Generalized scattering angles (μ, τ) from a cylinder as the two degrees of freedom in the double-bounce scattering mechanisms. (b) Angles (γ, δ) describing a general cylinder tilt.

$R(\gamma, \delta) \hat{c}$. As before, the incident wave vector is $\hat{k}_i(\theta_i, \phi_i)$, and the electric field in the (v, h, k) basis is $\vec{e}_i = (e_v^i, e_h^i, 0)$. The transformations that we apply to \vec{e}_i are as follows.

- 1) Bring \vec{e}_i into the (x, y, z) basis, i.e., apply $P(\theta_i, \phi_i)$.
- 2) Rotate the coordinate axis such that the cylinder is horizontal, i.e., apply $R(\gamma, \delta)$. Also, apply the rotation to \hat{k}_i , which gives $\hat{k}_i^c(\theta_i^c, \phi_i^c) = R(\gamma, \delta) \hat{k}_i(\theta_i, \phi_i)$ and thus determines the new wave vector direction (θ_i^c, ϕ_i^c) .
- 3) Bring the electric field back into the (v, h, k) basis, i.e., apply $P^{-1}(\theta_i^c, \phi_i^c)$.
- 4) Scatter the wave from the cylinder in a direction of choice (μ, τ) , i.e., apply $S_c(\mu, \tau; \theta_i^c, \phi_i^c)$, which is the scattering matrix for an upright cylinder.
- 5) Bring the electric field to the (x, y, z) basis, i.e., apply $P(\mu, \tau)$.
- 6) Undo the rotation of step 2, i.e., apply $R^{-1}(\gamma, \delta)$. This implies that the wave vector is now given by $\hat{k}_s^c(\theta_s^c, \phi_s^c) = R^{-1}(\gamma, \delta) \hat{k}_s^c(\mu, \tau)$.
- 7) Now, rotate the coordinate axis such that the ground is horizontal, i.e., apply $R(\alpha, \beta)$. Also, apply the rotation to \hat{k}_s^c , which gives $\hat{k}_s^g(\theta_s^g, \phi_s^g) = R(\alpha, \beta) \hat{k}_s^c(\theta_s^c, \phi_s^c)$ and thus determines the new wave vector direction (θ_s^g, ϕ_s^g) .
- 8) Bring the electric field back to the (v, h, k) basis, i.e., apply $P^{-1}(\theta_s^g, \phi_s^g)$.
- 9) Scatter the wave in the direction (θ_s^g, ϕ_s^g) , i.e., apply $S_g(\theta_s^g, \phi_s^g; \theta_i^g, \phi_i^g)$, which is the scattering matrix for a horizontal ground. The angles (θ_s^g, ϕ_s^g) must be such that, when we undo the rotation of step 7, the resulting wave vector is in the (known) backscatter direction (θ_s, ϕ_s) , i.e., $\hat{k}_s^s(\theta_s^s, \phi_s^s) = R(\alpha, \beta) \hat{k}_s(\theta_s, \phi_s)$.
- 10) Bring the electric field to the (x, y, z) basis, i.e., apply $P(\theta_s^g, \phi_s^g)$.
- 11) Undo the rotation of step 7, i.e., apply $R^{-1}(\alpha, \beta)$. This implies that the wave vector has been brought back to the backscattered direction with $\hat{k}_s(\theta_s, \phi_s) = R^{-1}(\alpha, \beta) \hat{k}_s^g(\theta_s^g, \phi_s^g)$.
- 12) Finally, bring the electric field back to the (v, h, k) basis, i.e., apply $P^{-1}(\theta_s, \phi_s)$.



Fig. 8. OJP forest for which tree and ground parameters were measured during CanEx-SM10. The respective vegetation parameters used for modeling are given in Table I.

Thus, the scattered electric field, $\vec{e}_s = (e_v^s, e_h^s, 0)$ is given by the following sequence of matrix multiplications:

$$\begin{aligned} \vec{e}_s = & \{ P^{-1}(\theta_s, \phi_s) R^{-1}(\alpha, \beta) P(\theta_s^g, \phi_s^g) S_g(\theta_s^g, \phi_s^g; \theta_i^g, \phi_i^g) \\ & \cdot P^{-1}(\theta_i^g, \phi_i^g) R(\alpha, \beta) R^{-1}(\gamma, \delta) P(\mu, \tau) \\ & \cdot S_c(\mu, \tau; \theta_i^c, \phi_i^c) P^{-1}(\theta_i^c, \phi_i^c) R(\gamma, \delta) P(\theta_i, \phi_i) \} \vec{e}_i. \quad (9) \end{aligned}$$

For the special case of a vertical trunk on a nonhorizontal ground, (9) can be simplified by setting the rotation matrix associated with the cylinder to identity ($R(\gamma, \delta) = \mathcal{I}$). As a result, $(\theta_i^c, \phi_i^c) = (\theta_i, \phi_i)$, also $(\theta_s^c, \phi_s^c) = (\mu, \tau)$, and the scattering matrix for an upright cylinder immediately applies to \vec{e}_i . In effect, we skip steps 1, 2, 3, and 6 in the aforementioned procedure, which results in

$$\begin{aligned} \vec{e}_s = & \{ P^{-1}(\theta_s, \phi_s) R^{-1}(\alpha, \beta) P(\theta_s^g, \phi_s^g) S_g(\theta_s^g, \phi_s^g; \theta_i^g, \phi_i^g) \\ & \cdot P^{-1}(\theta_i^g, \phi_i^g) R(\alpha, \beta) P(\mu, \tau) S_c(\mu, \tau; \theta_i, \phi_i) \} \vec{e}_i. \quad (10) \end{aligned}$$

With these theoretical definitions, the four scattering mechanisms can be described in the presence of nonflat topography.

IV. IMPLEMENTATION OF MODIFIED SCATTERING MECHANISMS

The implementation of the adjustment for terrain topography for the branch volume (B) and for the rough ground surface (G) scattering mechanisms is straightforward. The implementation for the double-bounce interactions (TG and BG) is more involved since there are two degrees of freedom to be considered. The simplest implementation is to find the backscattered wave as the succession of two scattering paths: 1) specular scattering at the trunk (*skirt* scattering pattern) followed by nonspecular scattering at the ground (non-*cone* scattering pattern) and 2) nonspecular scattering at the trunk (non-*skirt* scattering pattern) followed by specular scattering at the ground (*cone* scattering pattern). When the parameters that determine the vegetation, soil, and slope are known, it is possible to calculate the angles resulting in the exact two scattering paths, which are then used in the respective trunk-ground and branch-ground double-bounce calculations. However, as both scattering events—at the cylinder and the ground—are not simply delta functions, we must integrate over a range of intermediate scattering angles around the two scattering events; this permits

TABLE I
VEGETATION PARAMETER FOR AN OJP FOREST BASED ON MEASUREMENTS COLLECTED DURING CANEX-SM2010. TREES ARE MODELED WITH TRUNKS, LARGE BRANCHES (LB), SMALL BRANCHES (SB), AND NEEDLES

Parameter	Meas. Value	Parameter	Meas. Value
Canopy Height	11.4 m	SB Orientation	70°
LB Dielectric	32-j4	Needle Dielectric	32-j4
LB Length	1.2 m	Needle Length	3 cm
LB Radius	0.66 cm	Needle Radius	0.15 cm
LB Density	7/m ³	Needle Density	1728/m ³
LB Orientation	80°	Trunk Dielectric	36-j2
SB Dielectric	32-j4	Trunk Length	2.0 m
SB Length	0.8 m	Trunk Radius	6.8 (± 1.5) cm
SB Radius	0.46 cm	Trunk Density	0.25/m ²
SB Density	70/m ³		

a flexible and modular implementation. Nonspecular scattering paths are not expected to contribute considerably to the overall scattering return as the scattered power at non-*skirt* and non-*cone* scattering angles is negligible.

The scattering matrix of the ground is computed using the SEBCM method [14]. Note that a coherent ground scattering model including all orders of scattering from the ground is needed because the complex scattering matrix must be used to implement the successive scattering events shown in (9). The SEBCM is run with the respective soil conditions (soil layers, soil texture, and soil roughness) to generate the general full scattering matrix of the ground. This can be very time intensive. The SEBCM provides a full scattering matrix for the 3-D scattering problem of a layered ground with rough interfaces, which can be used as a look-up table for any incidence and scattering angle. Since the SEBCM is based on discrete Floquet modes, the final scattering matrix is interpolated such that incidence and scattering angles at any arbitrary interpolation interval are available.

To setup a realistic simulation as discussed in more detail in the next section, the radar incidence angle is assumed to be $\theta_i = 40^\circ$. The incidence and scattering angles are interpolated to be at 1° within $\pm 10^\circ$ of $\theta_i = 40^\circ$ and $\theta_s = 140^\circ$. All other angles are spaced at 5° . The scattering matrix of the ground is provided to the multispecies vegetation model, and depending on the slope of each pixel, the correct scattering matrix for the different scattering moments is selected. Two scattering mechanisms involve the ground: direct ground (G) and double-bounce (TG and BG) scattering. For both scattering mechanisms, the ground scattering matrix provided by SEBCM is used.

V. NUMERICAL RESULTS

To illustrate the impact of terrain topography on radar backscattering cross sections for vegetated terrain, a realistic simulation is set up. In support of investigations related to the AirMOSS mission, we consider a P-band radar at an incidence angle of 40° with a land cover type of evergreen forest, although any other microwave frequency and/or land cover type can be used. For the purpose of this sample simulation, the measured parameter of an Old Jack Pine (OJP) forest collected during the Canadian Experiment for Soil Moisture in 2010 (CanEx-SM10) [16] is used. A photograph of the modeled OJP forest is shown in Fig. 8. The vegetation parameters are given in Table I [13]. It is noted that the range of trunk radii is set to $\pm 22\%$ of the mean trunk radius, which is the standard

deviation calculated from field measurements. The soil profile is represented using 20 homogeneous soil layers and parameterized based on *in situ* measurements at the OJP AirMOSS study site. The soil texture composition is based on the Digital General Soil Map of the United States (STATSGO2) gap-filled Soil Survey Geographic Database (SSURGO) data [17]. The necessary information to utilize the dielectric soil model by Peplinski *et al.* [18] is as follows: a volumetric soil moisture of $0.05 \text{ cm}^3/\text{cm}^3$ is assumed for all 20 soil layers, with each soil layer defined with 68% sand, 10% clay, $1\text{-g}/\text{cm}^3$ bulk density, 10°C soil temperature, and $4\text{-g}/\text{cm}^3$ soil salinity. The root-mean-square height of the surface soil roughness is set to 0.02 m, and the surface correlation length is set to 12.5 times the surface soil roughness, both based on field observations.

The simulation results showing the effect of a ground surface tilt described with (α, β) in degrees are presented in Fig. 9. The predicted P-band radar backscatter coefficients for HH, VV, and HV in decibels are broken down to show the volume (B), ground (G), and trunk-ground double-bounce (TG) scattering mechanisms, as well as the total radar backscattering coefficient (Total) in decibels. The branch-ground double-bounce (BG) contribution is consistently smaller than -40 dB and is not shown. For each scattering mechanism, the case with $\alpha = \beta = 0^\circ$ describes a scene with no slope. Simulation results show the impact of a 2-D slope for a range of tilt angles: $\alpha \pm 10^\circ$ and $\beta \pm 10^\circ$.

The volume scattering can be seen to decrease on the order of 0.6 dB for a tilted scene due to the adjusted vegetation layer thickness, as shown in Fig. 9(d)–(f). The tilting of the slope toward the radar (positive α) results in an increase in the adjusted vegetation layer thickness, as can be seen in Fig. 1, which, in turn, results in an increase in attenuation of the radar signal in the canopy layer and therefore an overall decrease of the volume scattering. The reverse is true for tilting of the slope away from the radar (negative α): the decrease in the adjusted vegetation layer thickness results in a decrease in canopy attenuation and therefore an overall increase in the volume scattering. A tilting of the slope out of the plane of incidence (positive or negative β) modifies the adjusted vegetation layer thickness only slightly for a range of $\alpha \pm 10^\circ$ and $\beta \pm 10^\circ$, and the volume scattering changes therefore only slowly [Fig. 9(d)–(f)].

The ground contribution varies when tilting in the plane of incidence for HH and VV, as shown in Fig. 9(g) and (h), and varies when tilting out of the plane of incidence for HV, as shown in Fig. 9(i). A tilting toward the radar (positive α) corresponds to a smaller local incidence angle and therefore results in an increase of backscatter from the ground in HH and VV [Fig. 9(g) and (h)]. A tilting away from the radar (negative α) results in a decrease of backscatter from the ground in HH and VV. Superimposed over this general trend is the modified canopy attenuation due to the adjusted vegetation layer thickness. A tilting toward or away from the radar (positive or negative α) has little effect in HV [Fig. 9(i)], as is to be expected from theory. A tilting out of plane (positive or negative β) has a large impact in HV, where it increases the radar backscatter from the ground. The impact on HH and VV is more subdued, but in general, a decreasing trend is observed. This is consistent with the backscatter behavior of SEBCM in backscatter direction [14]. For the ground contribution, a tilt of 10° in the plane of incidence results in 5–6 dB difference for

HH and VV [Fig. 9(g) and (h)], and a tilt of 10° out of the plane of incidence relates to a 35-dB difference in HV [Fig. 9(i)].

The trunk-ground double bounce is strongest for $\alpha = 0$. In this situation, the *skirt* scattering pattern of the cylinder perfectly coincides with the *cone* scattering pattern of the ground, creating a very strong specular backscatter. If α is kept zero and β is varied, the double-bounce mechanism stays strong since the *skirt* scattering pattern still picks up the *cone* scattering pattern of the ground. When α is slightly increased, the *cone* scattering pattern from the ground no longer has a prominent intersection with the *skirt* pattern from the cylinder, therefore greatly reducing the strength of the trunk-ground double-bounce scattering mechanism. For the trunk-ground double bounce, a 10° tilt in the plane of incidence corresponds to a decrease of up to 35 dB in HH, VV, and HV [Fig. 9(j)–(l)].

The total backscatter is the summation of the volume (B), ground (G), and trunk-ground double-bounce (TG) radar backscattering coefficients. It can be seen that the trunk-ground double bounce is the dominant scattering mechanism for this particular evergreen forest. A 10° tilt in the plane of incidence translates to a change of up to 15 dB in HH [Fig. 9(a)], 10 dB in VV [Fig. 9(b)], and 1.5 dB in HV [Fig. 9(c)] for the total radar backscatter. These trends are consistent with the analysis of van Zyl [10] for a forest over a sloped ground tilted only in the plane of incidence ($\beta = 0$); it shows a similar breakdown of the scattering mechanisms. The ground contribution increases for an increasing α , which is to be qualitatively expected, and has also been observed in van Zyl [10]. The SEBCM full-wave model is a more accurate and representative model than the approximate model used in [10] and accounts for all orders of scattering including the coherent bistatic scattering; it is therefore expected to result in more accurate prediction in our analysis.

VI. CONCLUSION

An existing multispecies multilayered radar scattering model [11] has been generalized to permit terrain topography at fine scales. A methodology for incorporating the effects of topography on four different scattering mechanisms has been developed, and the implementation is outlined. For the purpose of illustrating the impact of topography on radar scattering, a sample set of simulations for a 2-D slope with $\alpha \pm 10^\circ$ and $\beta \pm 10^\circ$ is presented. It must be mentioned that the simulation results presented are for P-band, in anticipation of future work involving validation of the terrain topography methodology with radar data from AirMOSS. That said, the methodology described in this work is entirely general and can be applied to any other frequency of interest.

The implications of this work are twofold: 1) it demonstrates that incorporating terrain topography is crucial for accurate radar forward modeling especially over forested areas, and 2) it demonstrates a systematic and modular approach by which topography can be incorporated into an existing forward model. All that is required of the model is the ability to compute the full bistatic scattering matrix for ground and trunks in standard orientation. This modular approach only requires matrix-vector products and hence is computationally efficient.

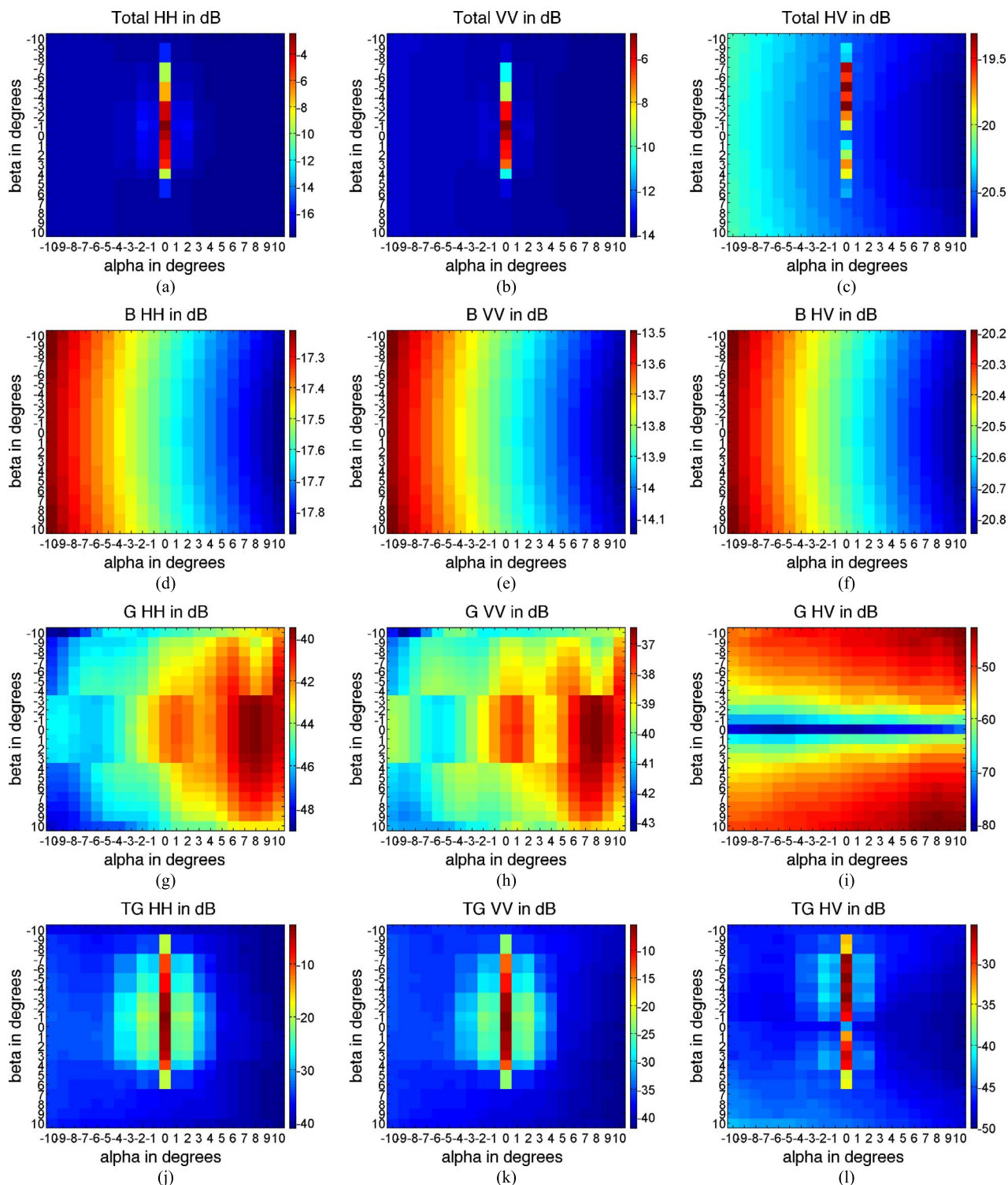


Fig. 9. Effect of ground surface tilt described with (α, β) in degrees. α is the tilt angle in the plane of incidence, and β is the tilt angle out of the plane of incidence. Predicted P-band radar backscatter coefficients for HH (left), VV (center), and HV (right) in decibels for total (Total), volume (B), ground (G), and trunk-ground double-bounce (TG) contributions. The branch-ground double-bounce (BG) contribution is less than -40 dB and is therefore not shown.

It can be anticipated that the incorporation of topography in radar scattering models will assist in radar-based estimations of soil moisture in hilly regions. This, in turn, will significantly aid in the prediction of areas susceptible to flash floods, as well as hydrologic land surface models at hill slope scales. Recent work has also demonstrated the importance of topography correction in radiometer models [19]. Combined with our work, such modifications can greatly enhance the scientific return from

combined radar-radiometer data, such as these obtained from the NASA Soil Moisture Active Passive mission.

REFERENCES

- [1] A. J. Luckman, "The effects of topography on mechanisms of radar backscatter from coniferous forest and upland pasture," *IEEE Trans. Geosci. Remote Sens.*, vol. 36, no. 5, pp. 1830–1834, Sep. 1998.
- [2] A. N. Flores, V. Y. Ivanov, D. Entekhabi, and R. L. Bras, "Impact of hillslope-scale organization of topography, soil moisture, soil temperature,

- and vegetation on modeling surface microwave radiation emission," *IEEE Trans. Geosci. Remote Sens.*, vol. 47, no. 8, pp. 2557–2571, Aug. 2009.
- [3] D. Entekhabi *et al.*, Eds. *SMAP Handbook: Soil Moisture Active and Passive*. Pasadena, CA, USA: National Aeronautics and Space Administration, Jet Propulsion Lab., JPL CL14-2285, JPL 400–1567, 2014.
- [4] A. Tabatabaenejad, M. Burgin, X. Duan, and M. Moghaddam, "P-band radar retrieval of subcanopy and subsurface soil moisture profile as a second-order polynomial: First AirMOSS results," *IEEE Trans. Geosci. Remote Sens.*, vol. 53, no. 2, pp. 645–658, Feb. 2015.
- [5] Y.-C. Lin and K. Sarabandi, "Electromagnetic scattering model for a tree trunk above a tilted ground plane," *IEEE Trans. Geosci. Remote Sens.*, vol. 33, no. 4, pp. 1063–1070, Jul. 1995.
- [6] J. M. Lopez-Sanchez, H. Esteban-Gonzalez, M. Baquero-Escudero, and J. Fortuny-Guasch, "An electromagnetic scattering model for multiple tree trunks above a tilted rough ground plane," *IEEE Trans. Geosci. Remote Sens.*, vol. 37, no. 2, pp. 659–667, Mar. 1999.
- [7] L. Tsang, K.-H. Ding, G. Zhang, C. C. Hsu, and J. A. Kong, "Backscattering enhancement and clustering effects of randomly distributed dielectric cylinders overlying a dielectric half space based on Monte-Carlo simulations," *IEEE Trans. Antennas Propag.*, vol. 43, no. 5, pp. 488–499, May 1995.
- [8] G. Smith-Jonforsen, L. M. H. Ulander, and X. Luo, "Low VHF-band backscatter from coniferous forests on sloping terrain," *IEEE Trans. Geosci. Remote Sens.*, vol. 43, no. 10, pp. 2246–2260, Oct. 2005.
- [9] S.-E. Park, W. M. Moon, and E. Pottier, "Assessment of scattering mechanism of polarimetric SAR signal from mountainous forest areas," *IEEE Trans. Geosci. Remote Sens.*, vol. 50, no. 11, pp. 4711–4719, Nov. 2012.
- [10] J. J. van Zyl, "The effect of topography on radar scattering from vegetated areas," *IEEE Trans. Geosci. Remote Sens.*, vol. 31, no. 1, pp. 153–160, Jan. 1993.
- [11] M. Burgin, D. Clewley, R. M. Lucas, and M. Moghaddam, "A generalized radar backscattering model based on wave theory for multilayer multi-species vegetation," *IEEE Trans. Geosci. Remote Sens.*, vol. 49, no. 12, pp. 4832–4845, Dec. 2011.
- [12] M. Moghaddam, S. Saatchi, and R. H. Cuenca, "Estimating subcanopy soil moisture with radar," *J. Geophys. Res., Atmos.*, vol. 105, no. D11, pp. 14899–14911, Jun. 2000.
- [13] A. Tabatabaenejad, M. Burgin, and M. Moghaddam, "Potential of L-band radar for retrieval of canopy and subcanopy parameters of boreal forests," *IEEE Trans. Geosci. Remote Sens.*, vol. 50, no. 6, pp. 2150–2160, Jun. 2012.
- [14] X. Duan and M. Moghaddam, "3-D vector electromagnetic scattering from arbitrary random rough surfaces using stabilized extended boundary condition method for remote sensing of soil moisture," *IEEE Trans. Geosci. Remote Sens.*, vol. 50, no. 1, pp. 87–103, Jan. 2012.
- [15] U. K. Khankhoje, M. Burgin, and M. Moghaddam, "On the accuracy of averaging radar backscattering coefficients for bare soils using the finite-element method," *IEEE Geosci. Remote Sens. Lett.*, vol. 11, no. 8, pp. 1345–1349, Aug. 2014.
- [16] R. Magagi *et al.*, "Canadian Experiment for Soil Moisture in 2010 (CanEx-SM10): Overview and preliminary results," *IEEE Trans. Geosci. Remote Sens.*, vol. 51, no. 1, pp. 347–363, Jan. 2013.
- [17] Soil Survey Staff, Natural Resources Conservation Service (NRCS), United States Department of Agriculture. Web Soil Survey, Accessed Feb. 10, 2016. [Online]. Available: <http://websoilsurvey.nrcs.usda.gov/>.
- [18] N. R. Peplinski, F. T. Ulaby, and M. C. Dobson, "Dielectric properties of soils in the 0.3–1.3-GHz range," *IEEE Trans. Geosci. Remote Sens.*, vol. 33, no. 3, pp. 803–807, May 1995.
- [19] X. Li, L. Zhang, L. Weihermüller, L. Jiang, and H. Vereecken, "Measurement and simulation of topographic effects on passive microwave remote sensing over mountain areas: A case study from the Tibetan plateau," *IEEE Trans. Geosci. Remote Sens.*, vol. 52, no. 2, pp. 1489–1501, Feb. 2014.



Mariko S. Burgin (S'09–M'14) received the M.S. degree in electrical engineering and information technology from the Swiss Federal Institute of Technology (ETH), Zurich, Switzerland, in 2008, and the M.S. and Ph.D. degrees in electrical engineering from the Radiation Laboratory, University of Michigan, Ann Arbor, MI, USA, in 2011 and 2014, respectively.

From 2014 to 2015, she was a Postdoctoral Scholar with the Water and Carbon Cycles (now Surface Hydrology) Group, Jet Propulsion Laboratory (JPL), California Institute of Technology, Pasadena, CA, USA. In 2016, she joined the Radar Science Group, JPL. Her research interests include theoretical and numerical studies of random media, development of forward and inverse scattering algorithms for geophysical parameter retrieval, and study of electromagnetic wave propagation and scattering properties of vegetated surfaces.



Uday K. Khankhoje (M'14) received the B.Tech. degree from the Indian Institute of Technology Bombay, Mumbai, India, in 2005 and the M.S. and Ph.D. degrees in electrical engineering from the California Institute of Technology (Caltech), Pasadena, CA, USA, in 2010.

He is an Assistant Professor of electrical engineering with the Indian Institute of Technology Delhi, New Delhi, India. He was a Caltech Postdoctoral Scholar with the Jet Propulsion Laboratory (NASA/Caltech) from 2011 to 2012 and a Postdoctoral Research Associate with the Department of Electrical Engineering, University of Southern California, Los Angeles, CA, from 2012 to 2013. His research interests lie in the area of computational electromagnetics and its applications to remote sensing and inverse imaging.



Xueyang Duan (S'07–M'12) received the B.Eng. degree in communication engineering from Shandong University, Jinan, China, in 2004, the M.S. degree in microelectronics, communications technology from the University of Ulm, Ulm, Germany, in 2006, and the M.S. degree in applied mathematics and the Ph.D. degree in electrical engineering from the University of Michigan, Ann Arbor, MI, USA, in 2010 and 2012, respectively.

From 2006 to 2007, she was a Development Engineer with the Test and Measurement Division, Rohde & Schwarz, Munich, Germany. She joined the Jet Propulsion Laboratory (JPL) as a Systems Engineer in 2014 after she spent two years as a Postdoctoral Research Associate with the Department of Electrical Engineering, University of Southern California, Los Angeles, CA, USA. Her research interests include forward and inverse modeling of electromagnetic scattering from layered rough surfaces with or without buried objects, radar system design, and radar measurements of vegetation and ground variables.



Mahta Moghaddam (S'86–M'87–SM'02–F'09) received the B.S. degree (with highest distinction) from the University of Kansas, Lawrence, KS, USA, in 1986 and the M.S. and Ph.D. degrees in electrical and computer engineering from the University of Illinois at Urbana-Champaign, Champaign, IL, USA, in 1989 and 1991, respectively.

She is a Professor of electrical engineering with the University of Southern California, Los Angeles, CA, USA. From 1991 to 2003, she was with the Radar Science and Engineering Section, NASA Jet Propulsion Laboratory, and from 2003 to 2011, she was a Professor of electrical engineering and computer science with the University of Michigan, Ann Arbor, MI, USA. She was a Systems Engineer for the Cassini Radar, the JPL Science Group Lead for the LightSAR project, and the Science Chair of the JPL Team X (Advanced Mission Studies Team). She is a member of the NASA Soil Moisture Active and Passive (SMAP) mission Science Team, a member of the NASA Advisory Council Earth Science Subcommittee, and the Principal Investigator of the AirMOSS Earth Ventures 1 mission. She has introduced new approaches for quantitative interpretation of multichannel radar imagery based on analytical inverse scattering techniques applied to complex and random media. Her most recent research interests include the development of new radar instrument and measurement technologies for subsurface and subcanopy characterization, development of forward and inverse scattering techniques of layered random media, and transforming concepts of radar remote sensing to near-field and medical imaging and therapy systems.

Dr. Moghaddam is the Editor-in-Chief of the IEEE ANTENNAS AND PROPAGATION MAGAZINE.